Supplementary Information

Pure and Pr-doped $Ce_4W_9O_{33}$ with superior hydroxyl scavenging ability: Humidity-independent oxide chemiresistors

Jun-Sik Kim,[a] Ki Beom Kim,[a] Hua-Yao Li,[b] Chan Woong Na,[c] Kyeorei Lim,[a] Young Kook Moon,[a] Ji Won Yoon,[a] Jong-Heun Lee[a,]*

[a]Department of Materials Science and Engineering, Korea University, Seoul 02841, Republic of Korea
[b]School of Optical and Electronic Information, Huazhong University of Science and Technology, 1037 Luoyu Road, Wuhan, Hubei, 430074, P. R. China
[c]Dongnam Regional Division, Korea Institute of Industrial Technology, Busan 46938, Republic of Korea
E-mail: jongheun@korea.ac.kr (Jong-Heun Lee)

EXPERIMENTAL SECTION

Sensing characteristics

Sensing materials and terpineol-based ink vehicles are mixed by mortar and pestle to get the viscous slurry (Materials:binder = 2:3 by weight). Sensors were fabricated by screen-printing of the slurry onto the alumina substrate (size: 1.5 × 1.5 mm^2, thickness: 0.25 mm) with two Au electrodes (electrode width: 1 mm, separation: 0.2 mm) on the top surface. Prior to measurements, sensor was annealed at 500 °C for 2 h to remove hydroxyl contents and stabilized the sensor. Electrometer with a computer was used to record DC 2-probe resistance of the sensor and temperature of the sensor was controlled by Ru micro-heater located on the bottom surface. Gas sensing characteristics were investigated at 200 – 400 °C to trimethylamine (TMA) in the different humidity condition and other interfering gases including acetone, ammonia (NH_3), benzene, ethanol, hydrogen (H_2), trimethylamine (TMA), xylene. Relative humidity of gas (temperature: 25 °C) was controlled by mixing synthetic dry air and synthetic humid air and concentration of gases were controlled by mixing synthetic dry/humid air and synthetic gases (100 ppm of gases in dry air balance). Synthetic humid air was generated by passing dry air through the water bubbler and the relative humidity was measured using a commercial humidity sensor. Flow rate was controlled by flow-through technique and fixed at 100 cm^3 min^{-1}.

Characterization

The morphology and microstructures of the specimens were investigated by a field-emission scanning electron microscope with an accelerating voltage of 15 kV (FE-SEM, SU-70, Hitachi) and field emission transmission electron microscopy with an accelerating voltage of 20 kV (FE-TEM, JEM-2100F, JEOL). Before SEM measurement, the specimens were sputtered with thin layers of platinum and TEM samples were prepared by a drop of an aqueous dispersion of particles on holey carbon grids. The N_2 adsorption–desorption isotherms were measured by using the surface area & porosity analyzer (Tristar 3000) at 77 K. The specific surface areas and the pore size distributions were calculated based on the Brunauer–Emmett–Teller (BET) and the Barret–Joyner–Halenda (BJH) models, respectively. X-ray diffraction pattern was recorded on powder specimens with a X-ray diffractometer (XRD, Rigaku, D/MAX-2500 V/PC with Cu Kα radiation) over the 2θ range of 20-80° at a scan rate of 4°m^{-1} to confirm the phase and crystallinity. Raman spectra was acquired with a Raman spectrometer (XperRam 200) with the excitation laser wavelength of 532 nm. The chemical states of the specimens were determined using X-ray photoelectron spectroscopy (XPS, VG Scientific ESCALAB 250) with an Al Kα radiation (1486.6 eV) source. The binding energies were calibrated by taking the C 1s peak at 284.6 eV as reference. Diffuse-reflectance Fourier transform IR spectra (DRIFTS) was recorded with Bruker Vertex 70-FTIR spectrometer equipped with a SMART collector and an MCT detector. The temperature and relative humidity of the test chamber used for DRIFT measurement were controlled by hot plate and synthetic humid air. Temperature programmed desorption (TPD) of O_2 were conducted in a flow rate of 50 ml min^{-1} of He (99.9999 %) and at a ramping rate of 10 °C min^{-1} (AutoChem II 2920, micromeritics). The sample powders (0.1g) were packed in a tubular quartz reactor connected to a thermal conductivity detector (TCD), pretreated at 300 °C for 1 hour in a flow of helium. Adsorption of oxygen was conducted at 350 °C for 1 hour in the flow of 5 % O_2/He. The temperature-programmed reduction (TPR) measurement was carried out with 10 % H_2/Ar. Prior to the experiment, 0.1 g of powder was calcined at 350 °C for 1 hour with a ramping rate of 10 °C min^{-1} in 5 % O_2/He, then cooled to 50 °C. TPR experiment was performed with 10 % H_2/Ar, the temperature being increased from 50 to 650 °C with a ramp rate of 10 °C min^{-1}. PL emission spectra were obtained using 325 nm He-Cd laser as excitation light source. The fluorescence spectra were recorded using a charge-coupled detector (PI-MAX3, USA) linked to a 0.5 m spectrometer (Spectrograph 500i, USA).

SUPPLEMENTARY FIGURES

Figure S1

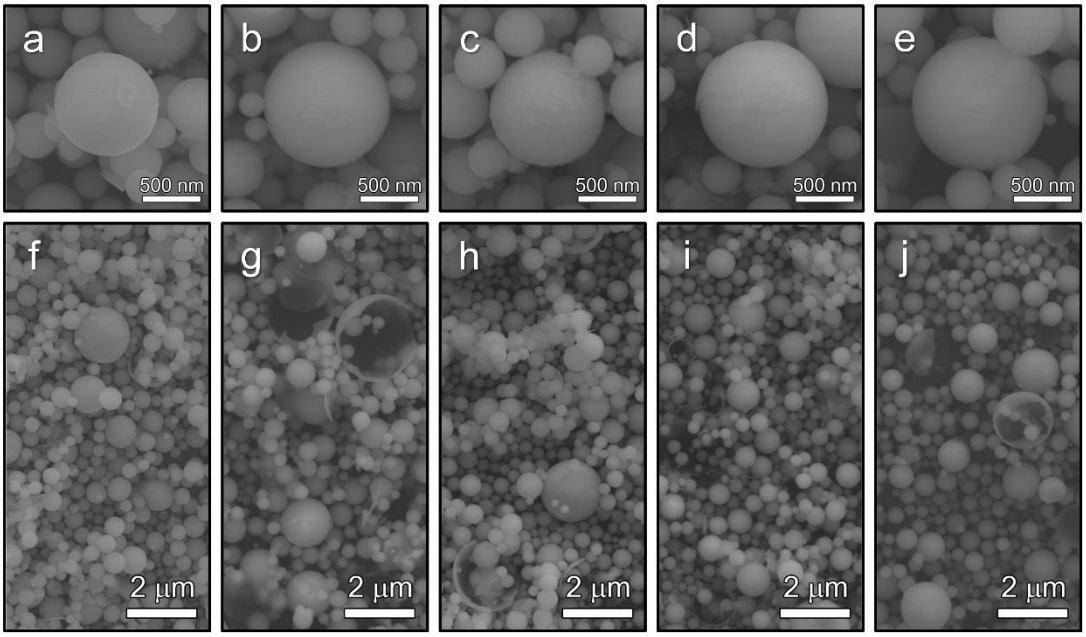

Figure S1 SEM images of as-prepared precursors for the preparation of (a, f) WO_3, (b, g) $Ce_4W_9O_{33}$, (c, h) $Pr_{0.1}Ce_{0.9}W$ (d, i) $Pr_{0.2}Ce_{0.8}W$, and (e, j) $Pr_{0.3}Ce_{0.7}W$.

Figure S2

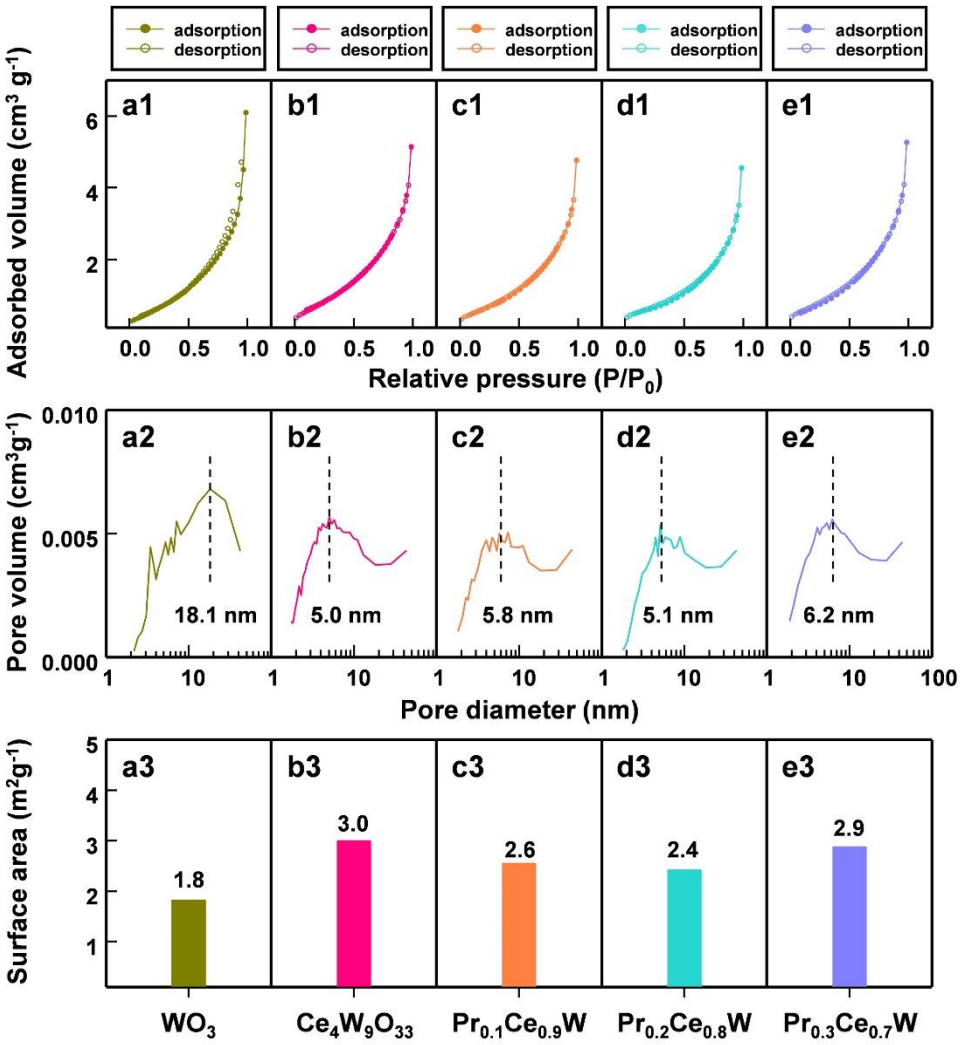

Figure S2 Ntirogen physisorption isotherm, pore size distribution, and specific surface area of (a) WO_3, (b) $Ce_4W_9O_{33}$, (c) $Pr_{0.1}Ce_{0.9}W$ (d) $Pr_{0.2}Ce_{0.8}W$, and (e) $Pr_{0.3}Ce_{0.7}W$.

Figure S3

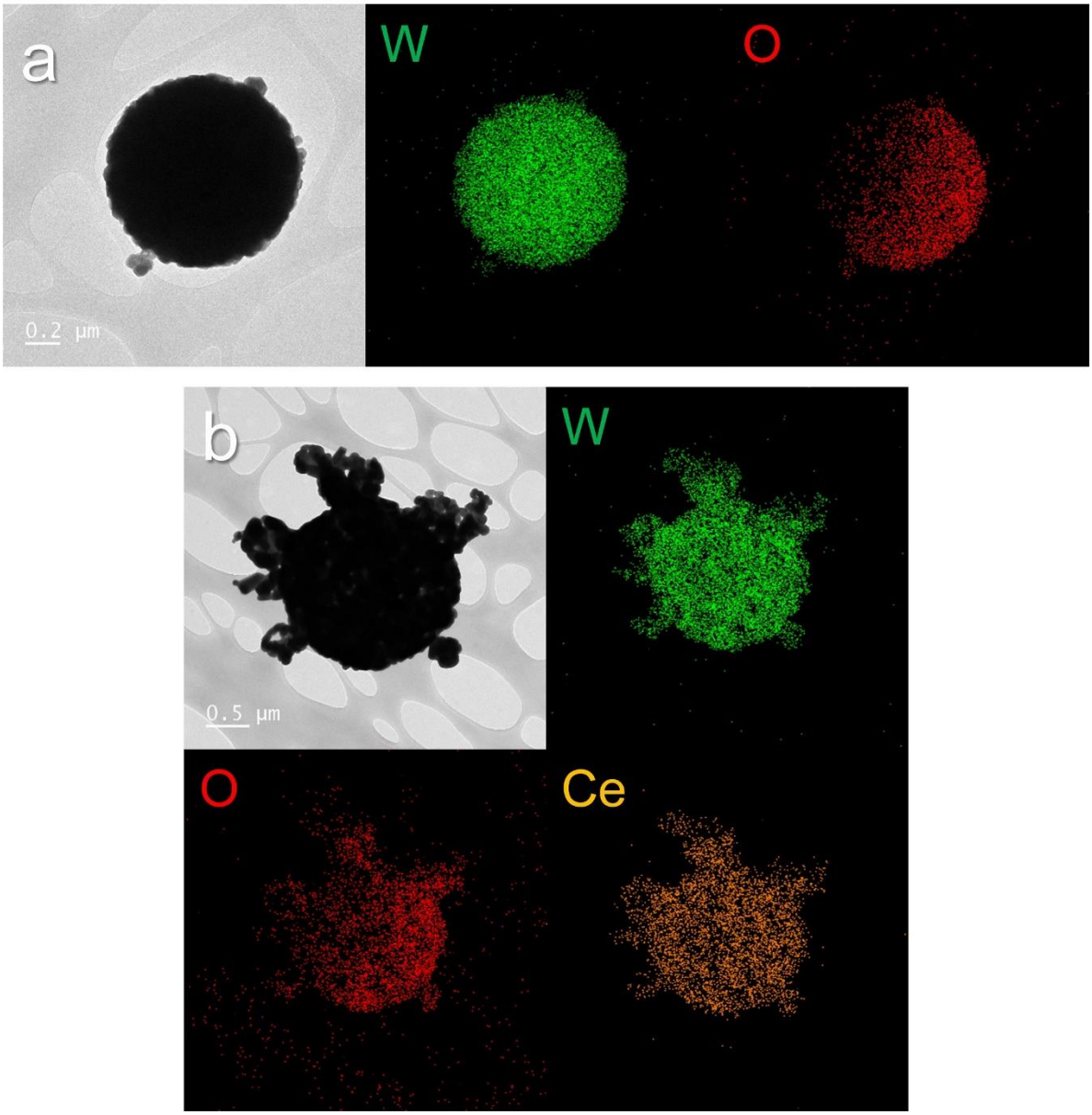

Figure S3 Elemental mapping of (a) WO_3 and (b) $Ce_4W_9O_{33}$.

Figure S4

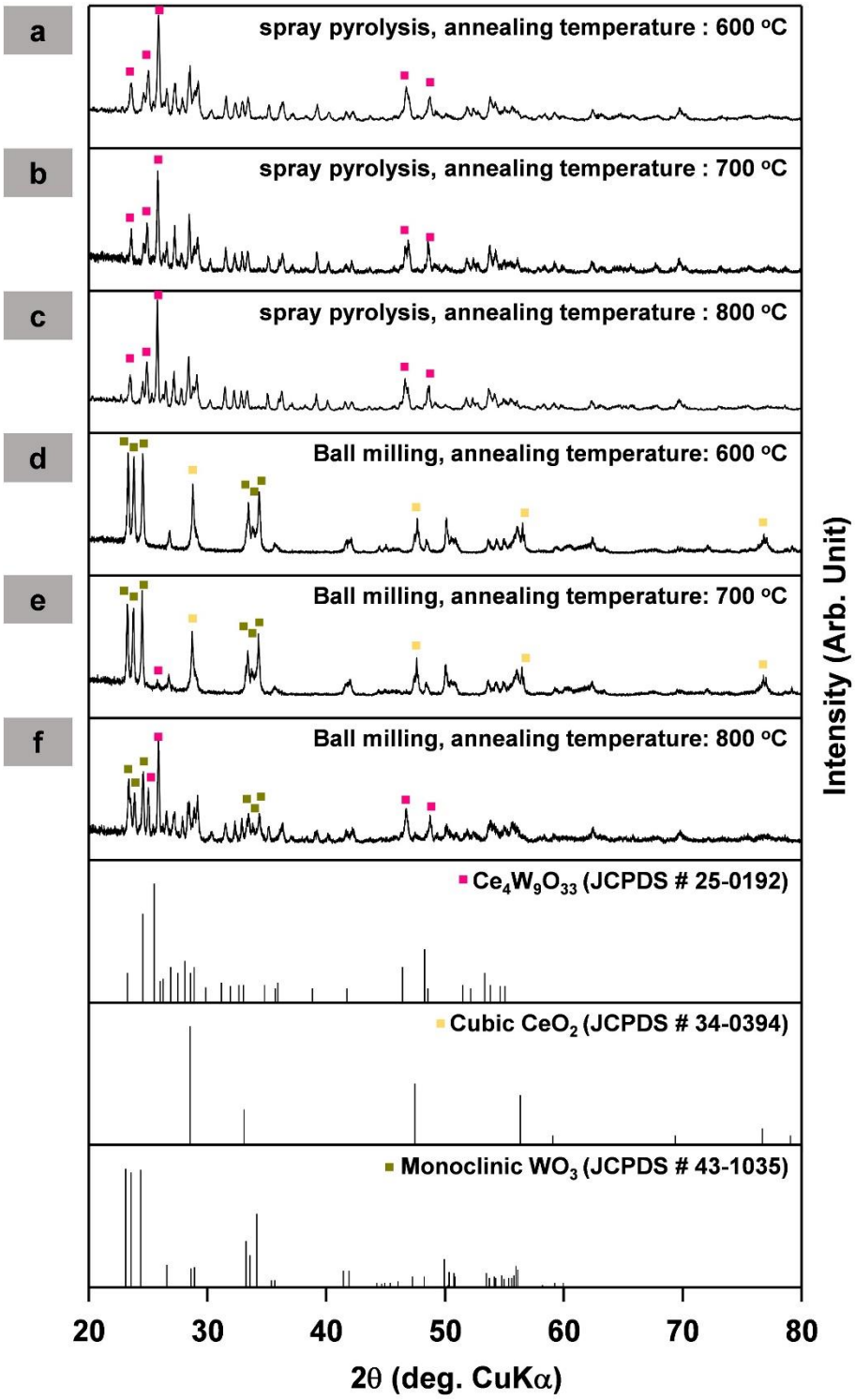

Figure S4 X-ray diffraction patterns of $Ce_4W_9O_{33}$ prepared by ultrasonic spray pyrolysis and subsequent annealing at (a) 600, (b) 700, and (c) 800 °C for 2h.; X-ray diffraction patterns of powders prepared by thermal annealing of ball-milled mixtures between CeO_2 and WO_3 (Ce:W=4:9) at (d) 600, (e) 700, and (f) 800 °C for 2 h.

Figure S5

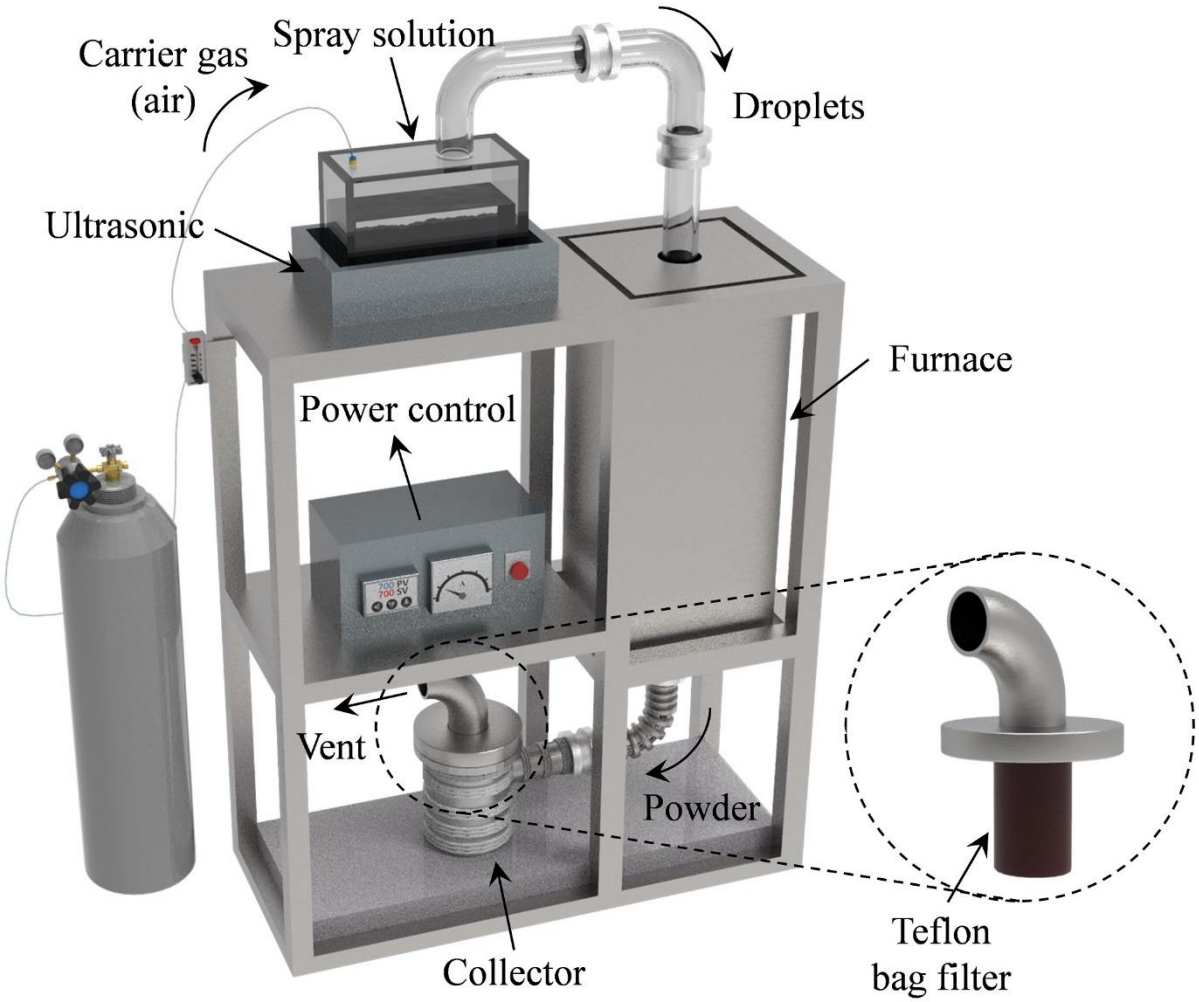

Figure S5 Schematic images of ultrasonic spray pyrolysis system.

Figure S6

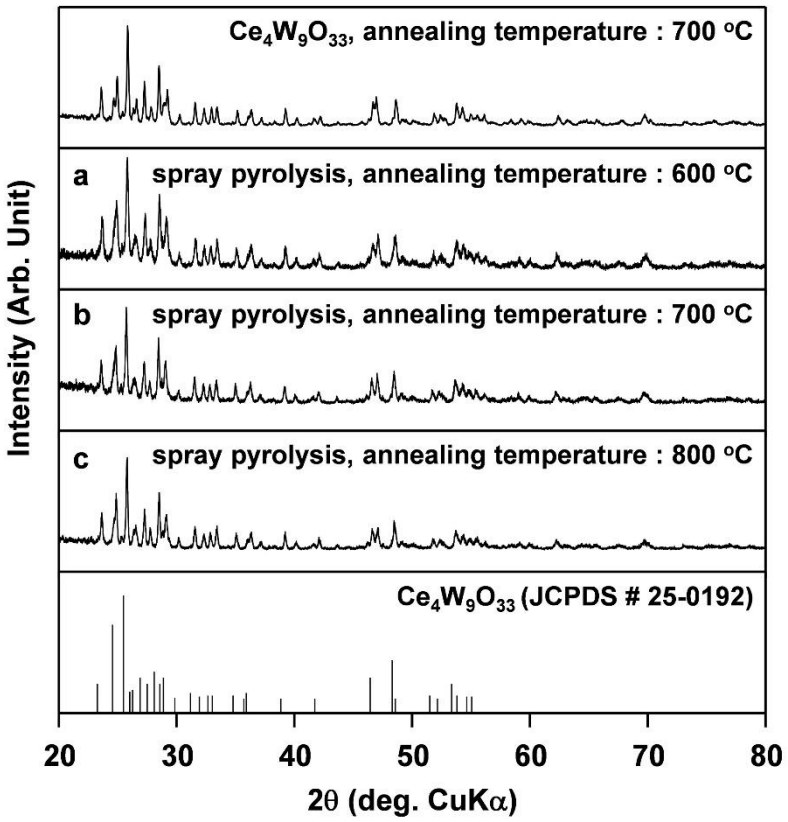

Figure S6 X-ray diffraction patterns of powders prepared by ultrasonic spray pyrolysis of aqueous solution containing Pr and W salts (Pr:W =4:9) and subsequent annealing at (a) 600, (b) 700, and (c) 800 °C for 2 h.

A specimen in which Pr and W metal salts were mixed in a ratio of 4:9 was synthesized in the same experimental procedure. XRD patterns of powders annealed at 600 – 800 °C were almost identical to the $Ce_4W_9O_{33}$ phase. This suggests that both Ce and Pr form a $2Ln_2O_3$-$9WO_3$ ($Ln_4W_9O_{33}$) phase (Ln = Ce, Pr) occupying the same sites which allow substitutional doping each other. Yoshimura et al.[S1] suggested that $2Pr_2O_3$-$9WO_3$ is also stable phase in the Pr_2O_3-WO_3 system but X-ray diffraction pattern of this phase has not been reported yet.

Figure S7

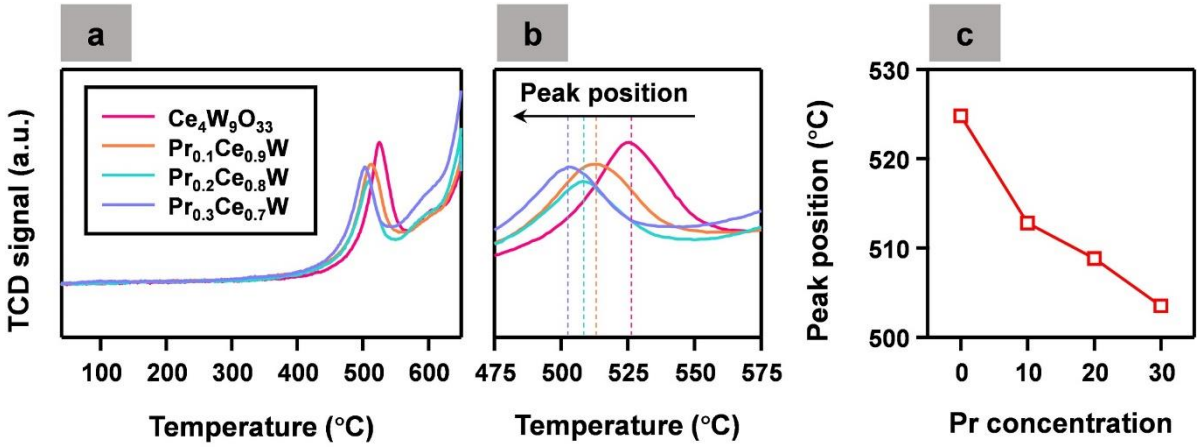

Figure S7 Thermal conductivity detector (TCD) signal of H_2-TPR analysis for (a, b) $Ce_4W_9O_{33}$ and Pr-doped $Ce_4W_9O_{33}$; (c) Peak position shift depending on the Pr concentration.

Figure S8

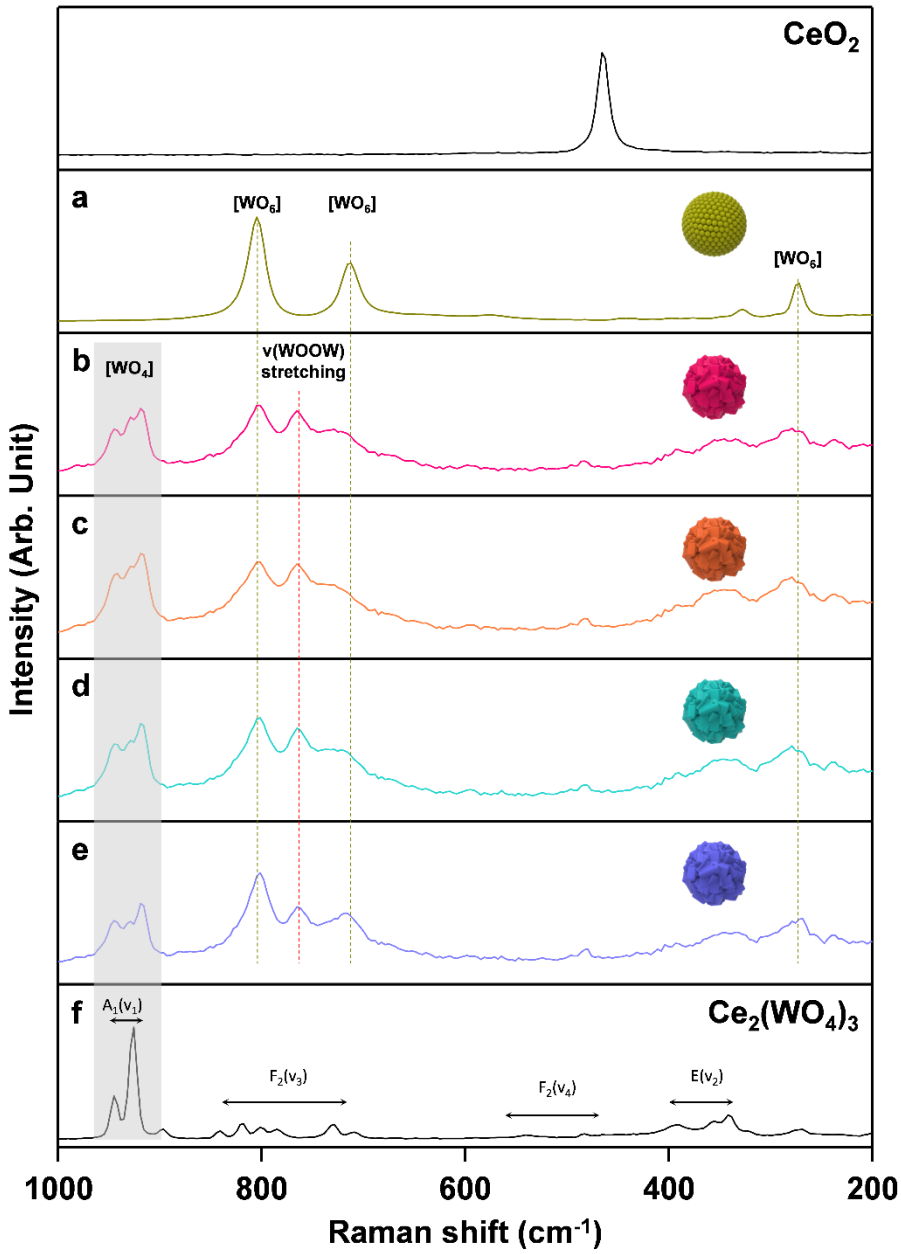

Figure S8 Raman spectra of (a) WO_3, (b) $Ce_4W_9O_{33}$, (c) $Pr_{0.1}Ce_{0.9}W$ (d) $Pr_{0.2}Ce_{0.8}W$, (e) $Pr_{0.3}Ce_{0.7}W$, and (f) $Ce_2(WO_4)_3$.

Raman spectra of CeO_2 and $Ce_2(WO_4)_3$ powders were examined as a reference spectra (CeO_2: commercial powders $Ce_2(WO_4)_3$: powders synthesized by spray pyrolysis using aqueous solution containing cerium and tungsten source [Ce:W = 2:3]). Raman spectra of the $Ce_4W_9O_{33}$ specimen showed the peaks of stretching mode and bending mode of the W-O-W bond of WO_6 units[S2,S3] but there is no peaks related to the fluorite CeO_2 lattice[S4] (Fig. S8b). Raman bands at the 767 cm^{-1} could be ascribed to the stretching mode of W-O-O-W vibration.[S5] Raman spectra of $Ce_2(WO_4)_3$ exhibited raman bands at 944 and 925 cm^{-1} assigned to two different types of WO_4 tetrahedrons in bravais cell.[S6] Therefore, additional peaks located at 900-1000 cm^{-1} in the Raman spectrum of $Ce_4W_9O_{33}$ highlighted in transparent grey box could be assigned WO_4 units known to exist in the $Ce_4W_9O_{33}$ lattice.[S7] As a result, $Ce_4W_9O_{33}$ lattice is expected to contain both [WO_4] and [WO_6] units joined by bridging WOOW and WOW bonds, but further study is needed for exact crystalline structure.

Pr doped $Ce_4W_9O_{33}$ showed similar Raman spectra to $Ce_4W_9O_{33}$, no additional peaks related to the Pr doping (Fig. S8c-e). However, in the $Pr_{0.3}Ce_{0.7}W$spectra, there is strong increase in the stretching modes of W-O-W bond of WO_6 units. This can be ascribed to the distortion of the lattice by Pr doping with different ionic radius and electronegativity. This result can be supported by O_2-TPD analysis in which oxygen desorption peak was abruptly increased in $Pr_{0.3}Ce_{0.7}W$specimen (Fig. S9b).

Figure S9

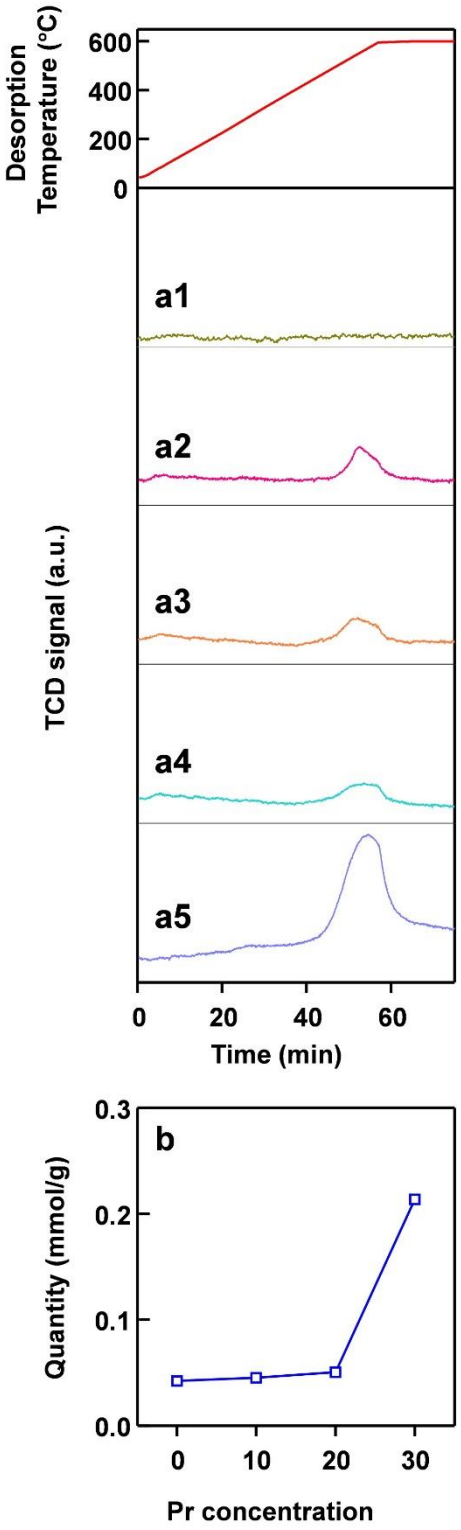

Figure S9 TCD signal of O_2-TPD analysis for (a1) WO_3, (a2) $Ce_4W_9O_{33}$, (a3) $Pr_{0.1}Ce_{0.9}W$ (a4) $Pr_{0.2}Ce_{0.8}W$ (a5) $Pr_{0.3}Ce_{0.7}W$.; (b) quantity of adsorbed oxygen.

Figure S10

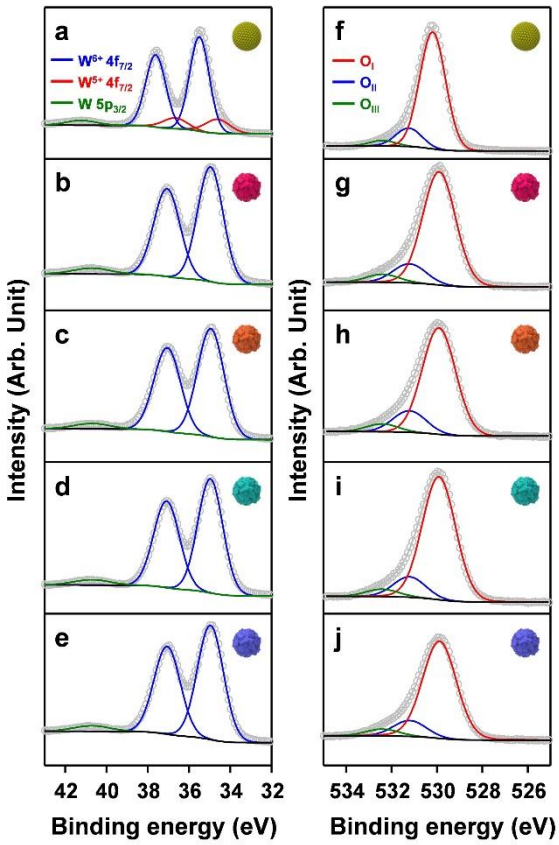

Figure S10 Fine scanned W 4f XPS spectra of (a) CeO_2, (b) $Ce_4W_9O_{33}$, (c) $Pr_{0.1}Ce_{0.9}W$ (d) $Pr_{0.2}Ce_{0.8}W$, and (e) $Pr_{0.3}Ce_{0.7}W$.; O 1s XPS spectra of (f) CeO_2, (g) $Ce_4W_9O_{33}$, (h) $Pr_{0.1}Ce_{0.9}W$ (i) $Pr_{0.2}Ce_{0.8}W$, and (j) $Pr_{0.3}Ce_{0.7}W$.

W 4f and O1s spectra of the WO_3, $Ce_4W_9O_{33}$, and Pr-doped $Ce_4W_9O_{33}$ were shown in the Figure S10. The W 4f spectra was peak fitted using voigt profile to satisfy the condition that spin-orbit separation is 2.1 eV and the area ratio of W $4f_{5/2}$ and W $4f_{7/2}$ doublets is 3:4. W 4f XPS spectrum of the WO_3 showed strong peaks at the 35.5 and 37.6 eV which can be attributed to the W^{6+} components and also showed W^{5+} related peaks at 34.6 and 36.7 eV (Fig. S10a). Most of the W element is considered to be W^{6+} with small amount of W^{5+} (15.1 %) in the WO_3 lattice. For the $Ce_4W_9O_{33}$ and Pr-doped $Ce_4W_9O_{33}$ specimens, W^{5+} related components were not observed, and the FWHM of W^{6+} components increased (FWHM of W^{6+} in WO_3: 1.1 eV, FWHM of W^{6+} in $Ce_4W_9O_{33}$ and Pr-doped $Ce_4W_9O_{33}$: 1.4 ~ 1.5 eV). No significant change of the W 4f spectra was observed as the Pr concentration increases (Fig. S10c-e). The O 1s spectra of the specimens were shown in the Figure S10f-j and curve-fitted into 3 peaks (O_I: lattice oxygen, O_{II}: hydroxyl or adsorbed oxygen, O_{III}: H_2O). The position of the O_I peak by lattice oxygen was located at 530.2 eV for WO_3, and 529.9 eV for $Ce_4W_9O_{33}$ and Pr-doped $Ce_4W_9O_{33}$ samples, and there was no significant difference in the peak positions for O_{II} and O_{III}. In all samples, oxygen was mostly present as lattice oxygen, and the differences in amount of lattice oxygen were not large (78.6 ~ 83.0 %), and the FWHM values increased from 1.3 eV in the WO_3 sample to 1.7 eV in the other samples.

Figure S11

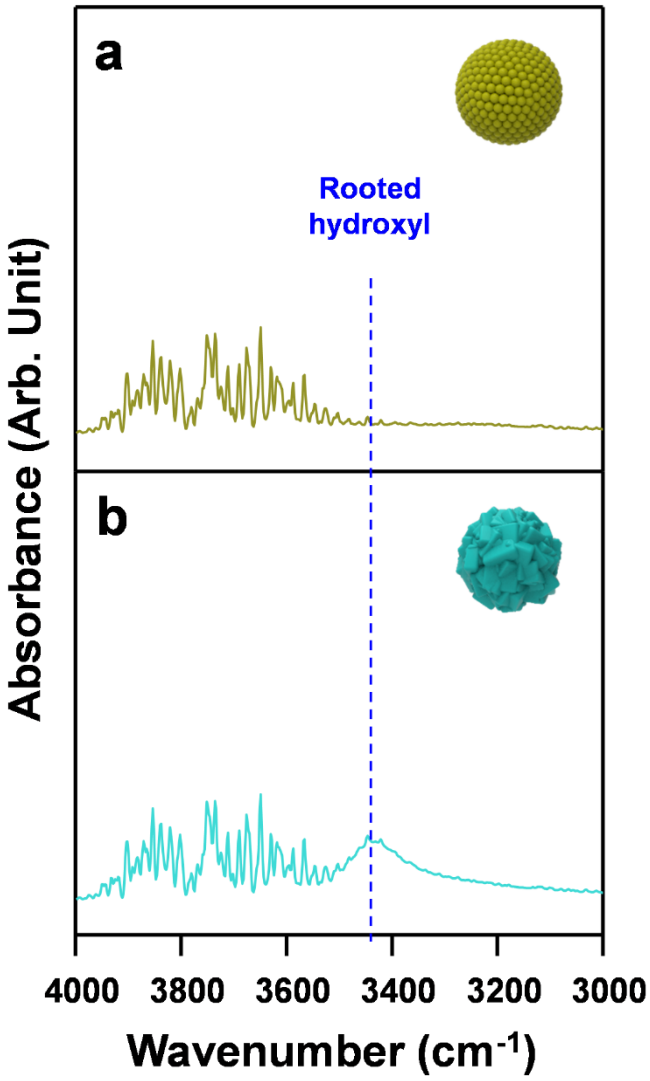

Figure S11 Absorbance of (a) WO_3 and (b) $Pr_{0.2}Ce_{0.8}W$ in RH 80% referenced to RH 0% by DRIFT analysis at 350 °C.

Figure S12

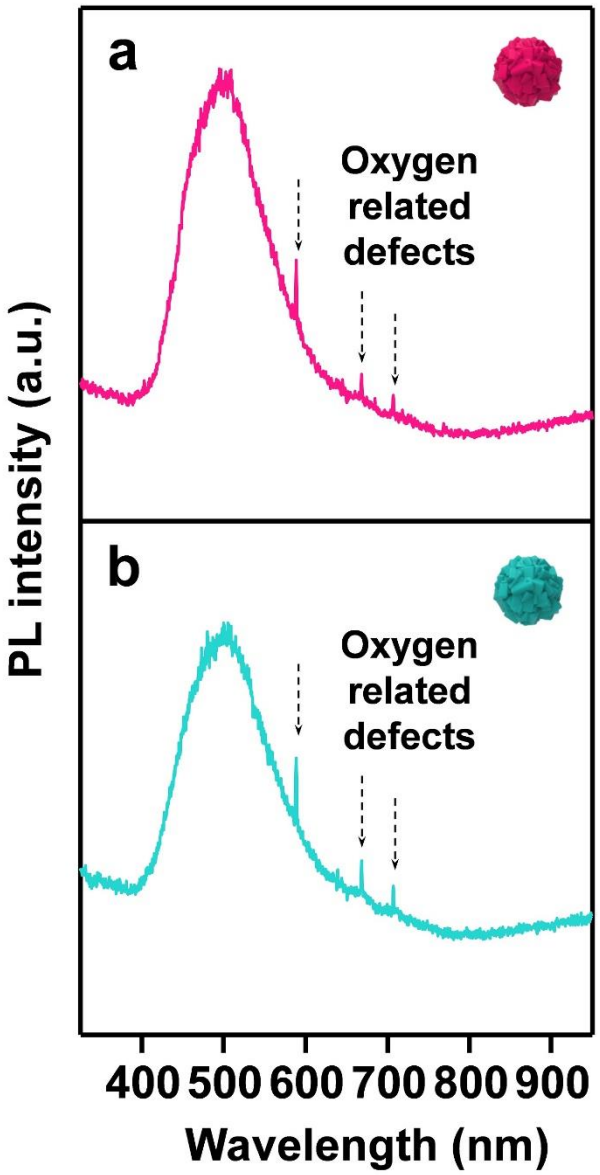

Figure S12 PL spectra of (a) $Ce_4W_9O_{33}$ and (b) $Pr_{0.2}Ce_{0.8}W$.

Figure S13

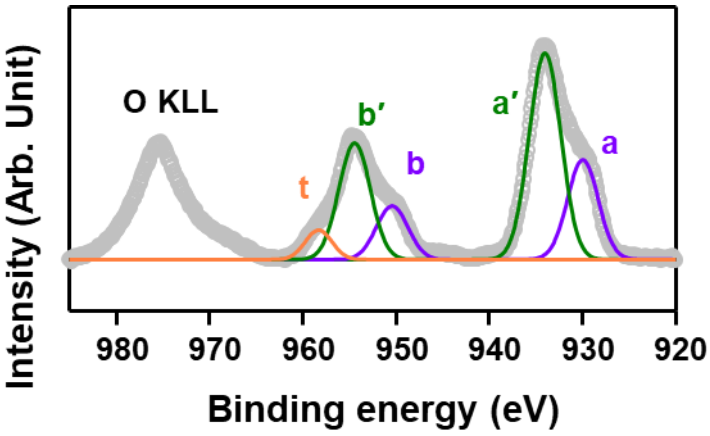

Figure S13 Fine scanned XPS Pr 3d spectra of $Pr_4W_9O_{33}$.

Figure S14

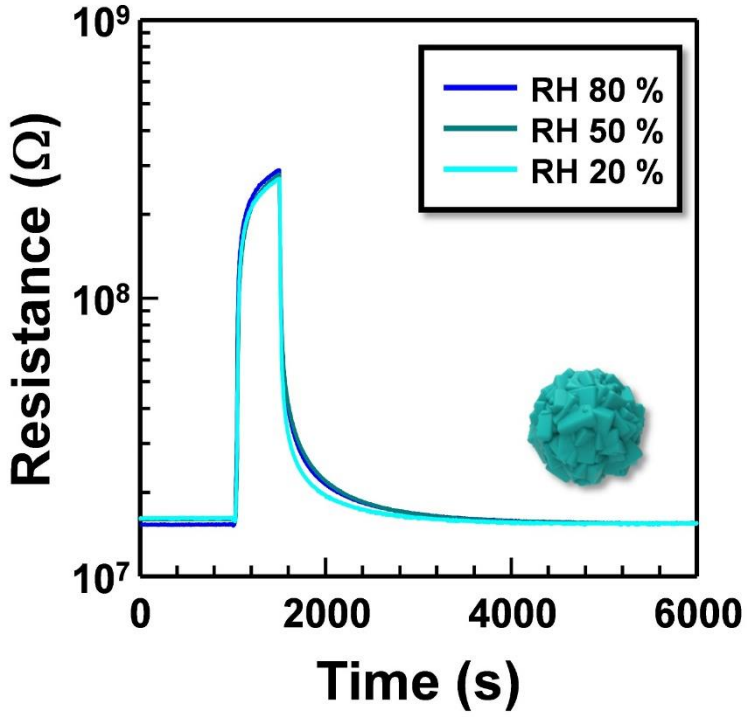

Figure S14 Dynamic sensing transients of $Pr_{0.2}Ce_{0.8}W$ sensor to 20 ppm TMA in different humidity conditions (RH 20, 50, and 80 %) at 350 °C.

Table S1 Humidity independent sensing characteristics of gas sensors using lanthanide elements in the literature.[S8-S11]

Sensing materials	Type	Operating temperature (°C)	Target gas	Concentration (ppm)	Resistance ratio ($R_{a\text{-}humid}/R_{a\text{-}dry}$) (%)	Gas response		Reference
						dry	Humid (RH 80 %)	
CeO_2-loaded In_2O_3	N	450	Acetone	20	98.7	4.7	4.5	[S8]
Tb-doped SnO_2	N	450	Acetone	20	76.7	15.9	12.7	[S9]
Pr-doped In_2O_3	N	450	Acetone	20	98.8	9.1	9.3	[S10]
Tb_4O_7-coated In_2O_3	N	400	Acetone	10	93.4	11.2	11.8	[S11]
$(Pr_{0.2}Ce_{0.8})_4W_9O_{33}$	**P**	**350**	**TMA**	**20**	**103.4**	**20.1**	**18.8**	**This study**

Table S2 XPS Ce 3d spectra peak table

Peak	v_0 (Ce^{3+})	v	v´ (Ce^{3+})	v´´	v´´´	u_0 (Ce^{3+})	u	u´ (Ce^{3+})	u´´	u´´´
Ce 3d peak BE values (eV)										
CeO_2	880.0	881.7	884.1	888.2	897.6	898.5	900.2	902.4	906.8	916.0
$Ce_4W_9O_{33}$	881.4	883.4	885.6	-	897.7	899.9	901.9	904.1	907.5	916.2
$Pr_{0.1}Ce_{0.9}W$	881.4	883.4	885.6	-	897.8	899.9	901.9	904.1	907.5	916.3
$Pr_{0.2}Ce_{0.8}W$	881.4	883.4	885.6	-	897.7	899.9	902.0	904.1	907.4	916.2
$Pr_{0.3}Ce_{0.7}W$	881.4	883.4	885.6	-	897.7	899.9	902.0	904.1	907.5	916.2
Area percentages I (%)										
CeO_2	2.43	13.8	17.33	11.31	14.99	1.61	8.85	11.5	7.81	10.37
$Ce_4W_9O_{33}$	19.54	5.16	32.23	-	1.18	13.33	3.52	22.14	2.08	0.81
$Pr_{0.1}Ce_{0.9}W$	20.29	4.83	32.55	-	1.33	13.24	3.28	21.65	1.94	0.90
$Pr_{0.2}Ce_{0.8}W$	20.52	4.76	32.68	-	1.45	13.40	3.24	21.34	1.66	0.95
$Pr_{0.3}Ce_{0.7}W$	20.10	5.49	31.46	-	1.62	13.54	3.73	20.90	2.07	1.08
FWHM (eV)										
CeO_2	1.8	1.7	4.0	3.6	1.9	1.8	1.6	4.1	3.5	1.9
$Ce_4W_9O_{33}$	3.1	2.3	3.7	-	2.4	3.1	2.3	3.7	2.4	2.4
$Pr_{0.1}Ce_{0.9}W$	3.1	2.3	3.7	-	2.4	3.1	2.3	3.7	2.4	2.4
$Pr_{0.2}Ce_{0.8}W$	3.1	2.3	3.7	-	2.4	3.1	2.3	3.7	2.4	2.4
$Pr_{0.3}Ce_{0.7}W$	3.1	2.3	3.7	-	2.4	3.1	2.3	3.7	2.4	2.4

Inter-component peak area ratios					
	Iv_0/Iu_0	Iv/Iu	Iv´/Iu´	Iv´´/Iu´´	Iv´´´/Iu´´´
CeO_2	1.51	1.56	1.51	1.45	1.45
$Ce_4W_9O_{33}$	1.47	1.47	1.46	-	1.46
$Pr_{0.1}Ce_{0.9}W$	1.53	1.47	1.50	-	1.48
$Pr_{0.2}Ce_{0.8}W$	1.53	1.47	1.53	-	1.53
$Pr_{0.3}Ce_{0.7}W$	1.48	1.47	1.51	-	1.50

Spin-orbit splitting (eV)					
	v_0/u_0	v/u	v´/u´	v´´/u´´	v´´´/u´´´
CeO_2	18.5	18.5	18.3	18.6	18.4
$Ce_4W_9O_{33}$	18.5	18.5	18.5	-	18.5
$Pr_{0.1}Ce_{0.9}W$	18.5	18.5	18.5	-	18.5
$Pr_{0.2}Ce_{0.8}W$	18.5	18.6	18.5	-	18.5
$Pr_{0.3}Ce_{0.7}W$	18.5	18.5	18.3	18.6	18.4

Table S3 XPS Pr 3d spectra peak table

Peaks	a	a´	a´´ (Pr^{4+})	b	b´	t	b´´ (Pr^{4+})
Pr 3d peak BE values (eV)							
Pr_6O_{11}	927.9	932.6	945.3	948.3	953.0	957.2	965.6
$Pr_{0.1}Ce_{0.9}W$	929.5	933.5	-	949.8	953.8	957.7	-
$Pr_{0.2}Ce_{0.8}W$	929.5	933.5	-	949.8	953.8	957.7	-
$Pr_{0.3}Ce_{0.7}W$	929.4	933.4	-	949.7	953.7	957.6	-
$Pr_4W_9O_{33}$	930.0	934.0	-	950.4	954.4	958.3	-
Area percentages I (%)							
Pr_6O_{11}	17.6	41.7	3.1	10.2	23.8	4.7	2.0
$Pr_{0.1}Ce_{0.9}W$	20.1	39.6	-	11.6	22.9	5.8	-
$Pr_{0.2}Ce_{0.8}W$	18.8	40.3	-	11.4	23.4	6.1	-
$Pr_{0.3}Ce_{0.7}W$	19.2	41.0	-	11.1	23.6	5.1	-
$Pr_4W_9O_{33}$	19.3	41.5	-	10.9	23.4	4.8	-
FWHM (eV)							
Pr_6O_{11}	3.5	4.6	3.1	3.6	4.7	3.9	3.1
$Pr_{0.1}Ce_{0.9}W$	4.0	4.0	-	4.0	4.0	3.3	-
$Pr_{0.2}Ce_{0.8}W$	4.0	4.0	-	4.0	4.0	3.3	-
$Pr_{0.3}Ce_{0.7}W$	4.0	4.0	-	4.0	4.0	3.3	-
$Pr_4W_9O_{33}$	4.0	4.0	-	4.0	4.0	3.3	-

Inter-component peak area ratios				
	Ia/Ib	Ia´/Ib´	(Ia+Ia´)/(Ib+Ib´+It)	Ia´´/Ib´´
Pr_6O_{11}	1.73	1.75	1.53	1.55
$Pr_{0.1}Ce_{0.9}W$	1.73	1.73	1.48	-
$Pr_{0.2}Ce_{0.8}W$	1.65	1.72	1.44	-
$Pr_{0.3}Ce_{0.7}W$	1.73	1.73	1.51	-
$Pr_4W_9O_{33}$	1.77	1.77	1.55	-

Spin-orbit splitting (eV)			
	a/b	a′/b′	a″/b″
Pr_6O_{11}	20.4	20.4	20.3
$Pr_{0.1}Ce_{0.9}W$	20.3	20.3	-
$Pr_{0.2}Ce_{0.8}W$	20.3	20.3	-
$Pr_{0.3}Ce_{0.7}W$	20.3	20.3	-
$Pr_4W_9O_{33}$	20.4	20.4	-

Inter-component peak area ratios of a″/b″ doublets is 1.55, which is characteristics of typical 3d orbital doublets. However, area ratios of a/b and a′/b′ doublets were 1.73 and 1.75, showing slightly higher values. And these values were similar to the 1.72, the area ratio of a/b and a′/b′ doublets presented by Borchert in the XPS Pr 3d spectra.[S12] Interestingly, the value of $(I_a+I_a')/(I_b+I_b'+I_t)$ including the structural factor (t) and two doublets (a/b, a′/b′) was 1.53, which was close to the 2:3 ratio of a typical 3d orbital.

REFERENCES

S1 M. Yoshimura, F. Sibieude, A. Rouanet and M. Foex, *J. Solid State Chem.*, 1976, **16**, 219–232.
S2 J. A. Horsley, I. E. Wachs, J. M. Brown, G. H. Via and F. D. Hardcastle, *J. Phys. Chem.*, 1987, **91**, 4014–4020.
S3 M. F. Daniel, B. Desbat and J. C. Lassegues, *J. Solid State Chem.*, 1987, **67**, 235–247.
S4 W. H. Weber, K. C. Hass and J. R. McBride, *Phys. Rev. B*, 1993, **48**, 178–185.
S5 L. Macalik, J. Hanuza and A. A. Kaminskii, *J. Mol. Struct.*, 2000, **555**, 289–297.
S6 L. J. Burcham and I. E. Wachs, *Spectroc. Acta Pt. A-Molec. Biomolec. Spectr.*, 1998, **54**, 1355–1368.
S7 M. Yoshimura, T. Sata, T. Nakamura, *Nippon Kagaku Kaishi*, 1973, **5**, 2287–2294.
S8 J.-W. Yoon, J.-S. Kim, T.-H. Kim, Y. J. Hong, Y. C. Kang and J.-H. Lee, *Small*, 2016, **12**, 4229–4240.
S9 C.-H. Kwak, T.-H. Kim, S.-Y. Jeong, J.-W. Yoon, J.-S. Kim and J.-H. Lee, *ACS Appl. Mater. Interfaces*, 2018, **10**, 18886–18894.
S10 J.-S. Kim, C. W. Na, C.-H. Kwak, H.-Y. Li, J. W. Yoon, J.-H. Kim, S.-Y. Jeong and J.-H. Lee, *ACS Appl. Mater. Interfaces*, 2019, **11**, 25322–25329.
S11 S.-Y. Jeong, Y. M. Moon, J. K. Kim, S.-W. Park, Y. K. Jo, Y. C. Kang and J.-H. Lee, *Adv. Funct. Mater.*, 2020, 2007895.
S12 H. Borchert, Y.V. Frolova, V. V. Kaichev, I. P. Prosvirin, G. M. Alikina, A. I. Lukashevich, V. I. Zaikovskii, E. M. Moroz, S. N. Trukhan, V. P. Ivanov, E. A. Paukshtis, V. I. Bukhtiyarov and V. A. Sadykov, *J. Phys. Chem. B*, 2005, **109**, 5728–5738.